

# Comparison of hydrogen diffusivities measured by electrochemical permeation and temperature-programmed desorption in cold-rolled pure iron

Alfredo Zafra<sup>a</sup>, Zachary Harris<sup>b</sup>, Chao Sun<sup>a</sup>, Emilio Martínez-Pañeda<sup>a,\*</sup>

<sup>a</sup>*Department of Civil and Environmental Engineering, Imperial College London, London SW7 2AZ, UK*

<sup>b</sup>*Department of Materials Science and Engineering, University of Virginia, Charlottesville, VA 22904, USA*

---

## Abstract

The diffusivity of hydrogen in cold-rolled pure iron is investigated using permeation and desorption methods. Electrochemical charging, electro-permeation and thermal desorption spectroscopy (TDS) experiments are conducted. Firstly, the relation between the charging current and the hydrogen concentration is established. Secondly, permeation experiments are conducted at 22, 40 and 67°C to quantify the diffusivity dependence on temperature. Finally, the diffusivity is estimated by using two types of desorption experiments and Fick's law: (i) a 'rest time' method, by which we measure the hydrogen content of samples held at room temperature for different times, and (ii) isothermal desorption experiments at temperatures ranging from 22 to 80°C, fitting the resulting desorption rate versus time curves. Good agreement is obtained between the isothermal desorption and permeation approaches, with observed differences discussed and rationalised. Moreover, measured diffusivity values for cold-rolled pure iron are also found to be comparable to those reported in the literature. This work demonstrates that isothermal desorption experiments are a convenient approach to determine hydrogen diffusivity over a wide range of temperatures, as facilitated by new TDS systems with fast heating rates.

---

\*Corresponding author.

*Email address:* e.martinez-paneda@imperial.ac.uk (Emilio Martínez-Pañeda)

*Keywords:*

Hydrogen, Electro-permeation, Diffusion, Thermal Desorption Spectroscopy,  
Isothermal desorption

---

## 1. Introduction

Hydrogen-induced degradation is a pertinent life-limiting damage mode for many metallic structural components across the aerospace, marine, energy, transportation, and infrastructure sectors (Gangloff, 2003). Critically, the presence of hydrogen-assisted sub-critical cracking compromises structural integrity management approaches, thereby complicating life prediction and fracture control efforts (Gangloff, 2003, 2016). Such effects become increasingly important as novel approaches to increasing the viability of hydrogen energy technologies are considered (Gangloff and Somerday, 2012), which may lead to existing infrastructure being subjected to unexpected operating conditions. For example, feasibility studies have suggested that blending hydrogen into natural gas pipeline networks is one pathway by which gaseous hydrogen may be economically stored and transported (Melaina et al., 2013; Hafsi et al., 2019; Ishaq and Dincer, 2020). However, recent experimental evaluations have also demonstrated that the exposure of pipeline steels to natural gas/hydrogen mixtures can result in accelerated fatigue crack growth rates (Meng et al., 2017; Shang et al., 2020), degraded fracture resistance (Nguyen et al., 2020), and reduced tensile properties (*e.g.*, breaking stress, notch tensile strength, ductility, etc.) (Meng et al., 2017). Critically, the extent of the degradation in mechanical properties is sensitive to the hydrogen volume fraction in the natural gas/hydrogen mixture, suggesting a fundamental dependence of the degradation mechanism on the available hydrogen content (Meng et al., 2017).

Driven by this deleterious impact on performance, over a century of scientific study (Johnson, 1875) has sought to mechanistically understand the microscale processes by which hydrogen degrades the mechanical properties of structural metals. These efforts have led to the development of numerous theories (Robertson et al., 2015; Gerberich, 2012; Shishvan et al., 2020), but a growing literature database strongly suggests that

hydrogen-induced degradation proceeds *via* the synergistic interaction of several different hydrogen-modified processes (Gangloff, 2017; Djukic et al., 2019; Robertson et al., 2015); *i.e.*, hydrogen-induced reductions in grain boundary cohesive strength (Harris et al., 2018; Kristensen et al., 2020), hydrogen-modified plasticity behavior (Barnoush and Vehoff, 2010; Nagao et al., 2018; Wang et al., 2014; Harris et al., 2020), hydrogen-induced stabilization of vacancies (Lawrence et al., 2017; Nagumo and Takai, 2019), *etc.*. Critically, the relative contributions of these various hydrogen-modified processes to material degradation are likely to evolve with changes in hydrogen content (Harris et al., 2018). As such, in addition to evaluating the operative hydrogen degradation mechanisms, it is equally important to develop a clear understanding of fundamental hydrogen-material interactions (*e.g.*, uptake, trapping, and diffusion) (Depover and Verbeken, 2021; Gangloff, 2017; Martínez-Pañeda et al., 2020). It is well-established that differences in hydrogen-material interactions alone can modify susceptibility to hydrogen-induced degradation (Nelson and Stein, 1973). For example, the magnitude of the Stage II crack growth rate commonly observed during hydrogen environment-assisted cracking in severe environments has been shown to linearly scale with differences in hydrogen diffusivity (Gangloff, 2008; Martínez-Pañeda et al., 2016; Harris et al., 2021a). Similarly, the threshold stress intensity for hydrogen-assisted cracking generally correlates well with the diffusible hydrogen concentration (Akhurst and Baker, 1981; Gangloff, 2017; Martínez-Pañeda et al., 2018). Lastly, for closed systems containing a finite hydrogen concentration, the introduction of a uniform distribution of strong hydrogen trap sites (such as carbides) has been demonstrated to reduce susceptibility *via* the sequestering of hydrogen into these benign locations (Bhadeshia, 2016; Fernández-Sousa et al., 2020).

Several different experimental approaches exist for quantifying hydrogen-metal interactions. For example, inert gas fusion methods are commonly employed to determine the total hydrogen content (Lawrenz and Mitchell, 2006), while the barnacle cell electrode method can be used to quantify the diffusible hydrogen content under electrochemical charging conditions (DeLuccia and Berman, 1981). However, the two most

common methods for assessing hydrogen-metal interactions are permeation and thermal desorption (Depover and Verbeken, 2021). Briefly, permeation experiments are conducted by separating two independent environments by means of a thin membrane made of the material of interest. Atomic hydrogen is generated and absorbed on one side of the membrane, it then diffuses through the membrane, and subsequently effuses out the other side. Permeation can be conducted using either gaseous or electrochemically generated hydrogen, with the former being common for measuring permeation at elevated temperatures (Johnson, 1988). For gaseous permeation, it is typical for the egress side of the membrane to be held under vacuum, so that the permeation rate of hydrogen can be monitored via mass spectrometer (Choi, 1970) or the change in vacuum pressure (Stross and Tompkins, 1956). For electrochemical permeation, the permeation rate is measured via the current induced by the oxidation of hydrogen as it effuses from the membrane (Subramanyan, 1981; Boes and Züchner, 1976). Conversely, thermal desorption-based methods typically use specimens that have been precharged with hydrogen, which are placed into a vacuum chamber and heated according to a pre-programmed temperature versus time profile (Verbeken, 2012). The hydrogen desorbing from the specimen is then measured by a mass spectrometer. Post-experiment analysis of the obtained permeation rate or desorbed hydrogen content versus time (or temperature) data is then conducted to determine information on hydrogen-metal interactions, such as hydrogen solubility, trapping, and diffusivity behavior (Galindo-Nava et al., 2017; Díaz et al., 2020a,b,c).

Given that desorption-based methods are predominantly performed on precharged specimens, the necessity of conducting the experiment under high vacuum conditions limits the utility of this approach for materials with a ‘fast’ hydrogen diffusivity (such as pure Fe). Specifically, while it is certainly possible to obtain information on the trapping behavior of such materials with desorption approaches (Choo and Lee, 1982, 1983; Lee and Lee, 1987), the rapid egress of the lattice hydrogen can obfuscate assessments of hydrogen solubility and diffusivity. As such, it is common for ‘fast’ diffusing materials to be characterized using permeation methods. However, permeation experiments can

exhibit substantial scatter. For example, hydrogen diffusivities determined from permeation experiments for nominally pure Fe at ambient temperature (25°C) can differ by multiple orders of magnitude across studies (Kumnick and Johnson, 1974). This significant variability in permeation-measured data has been attributed to a wide range of potential influences, including: testing variable sensitivities (Gonzalez, 1969; Turnbull, 1995), surface effects (Kiuchi and McLellan, 1983; Addach et al., 2009), nonsteady-state conditions (Nelson and Stein, 1973), concentration-dependent diffusion (Ono and Rosales, 1968; Zafra et al., 2020), hydrogen trapping (Kumnick and Johnson, 1974; Oriani, 1970), and analysis method (Boes and Züchner, 1976; Carvalho et al., 2017).

These aforementioned challenges associated with assessing the diffusivity of hydrogen in pure Fe using permeation experiments strongly motivate exploring the use of desorption-based approaches for ‘fast’ diffusing alloys. For example, isothermal desorption experiments have been used to generate hydrogen diffusivity versus temperature relationships in stainless steels (Mine et al., 2009), Ni-based superalloys (Ai et al., 2013), Cu-Ni and Ni-Cr (Matsuo et al., 2014), a number of low-alloy steels (Yamabe et al., 2015), and precipitation-hardened steels (Yamabe et al., 2021). Critically, in order to use this isothermal method for low-alloy steels, large specimens up to 19 mm in diameter were required (Yamabe et al., 2015). Recent advances in thermal desorption equipment, including improved conduction-based heating capabilities that can induce controlled heating rates of up to 60°C/min, vacuum systems with dedicated loading chambers for fast evacuation to reduce sample ‘rest time’, and improved resolution mass spectrometers, suggest that this desorption-based approach could be used to obtain near-ambient (< 100°C) hydrogen diffusivity data in ‘fast’ diffusing materials, such as pure iron, without the need for large specimens. However, such an evaluation and the follow-on comparison between isothermal desorption and permeation-determined diffusivities have yet to be performed.

The objective of this study is to compare permeation and thermal desorption-based assessments of hydrogen diffusivity using 1-mm thick cold-rolled pure iron to establish the efficacy of desorption-based approaches for measuring hydrogen diffusivities in a

representative ‘fast’ diffusing material. The total hydrogen concentration versus applied current density relationship is first established for cold-rolled pure iron to inform the current density to be employed in subsequent experiments. Permeation measurements are performed at temperatures ranging from 22 to 67°C and the hydrogen diffusivity is then estimated using three different approaches: breakthrough, lag time, and by fitting the permeation transient to an approximate solution of Fick’s law. These data are then compared to hydrogen diffusivity values determined from both variable rest time and isothermal (ranging from 22 to 80°C) desorption experiments. We extensively discuss differences and similarities, as well as the implications for diffusion data extraction.

## 2. Experimental Methods

### 2.1. Material

This study was conducted using cold-rolled pure iron (supplier-reported purity of >99.5 wt. %Fe) procured in the as-rolled condition from Goodfellow Ltd. as a 1-mm thick sheet. The supplier-reported average degree of cold work was 50%. All experiments were performed on thin plate specimens with nominal dimensions of 250 mm x 250 mm x 1 mm (electropermeation) and 10 mm x 10 mm x 1 mm (desorption), which were excised from the sheet using an abrasive saw. Each face of the sample was iteratively ground flat using SiC papers, finishing at 1200 grit.

### 2.2. Electropermeation

Electrochemical permeation experiments were performed at temperatures of 22, 40, and 67°C using a modified Devanathan-Stachurski double-cell that was capable of being submerged in a hot bath; a schematic of this system is shown in Fig. 1. Two tests were conducted for each temperature. A masking plate was used to consistently expose a circular area of 2 cm<sup>2</sup> (16-mm diameter) on the sample membrane to both sides of the double-cell. For the experiments conducted at 40 and 67°C, the hot bath temperature was actively regulated by a thermostat and continuously monitored with a thermometer, which was in contact with the specimen. This setup resulted in a

variation of  $\pm 1^\circ\text{C}$  in temperature over the course of a given permeation experiment. Note that the temperature of the solution at each side of the double-cell was allowed to stabilize prior to the start of each elevated temperature permeation experiment. The three-electrode hydrogen reduction cell was filled with 3 wt. % NaCl solution and contained a Pt counter electrode and a saturated calomel reference electrode. Hydrogen production was achieved by applying a current density of  $5\text{ mA/cm}^2$  to the cold-rolled Fe membrane using a Gamry 1010B potentiostat operated in galvanostatic mode. The hydrogen oxidation cell was filled with 0.1 M NaOH solution and also contained a Pt counter electrode and a saturated calomel reference electrode, with a second Gamry 1010B potentiostat operated in chronoamperometry mode to record the hydrogen permeation current density,  $J_p$ , as a function of time. The hydrogen reduction and oxidation reactions taking place at the entry and exit surfaces of the specimen, respectively, are also included in Fig. 1.

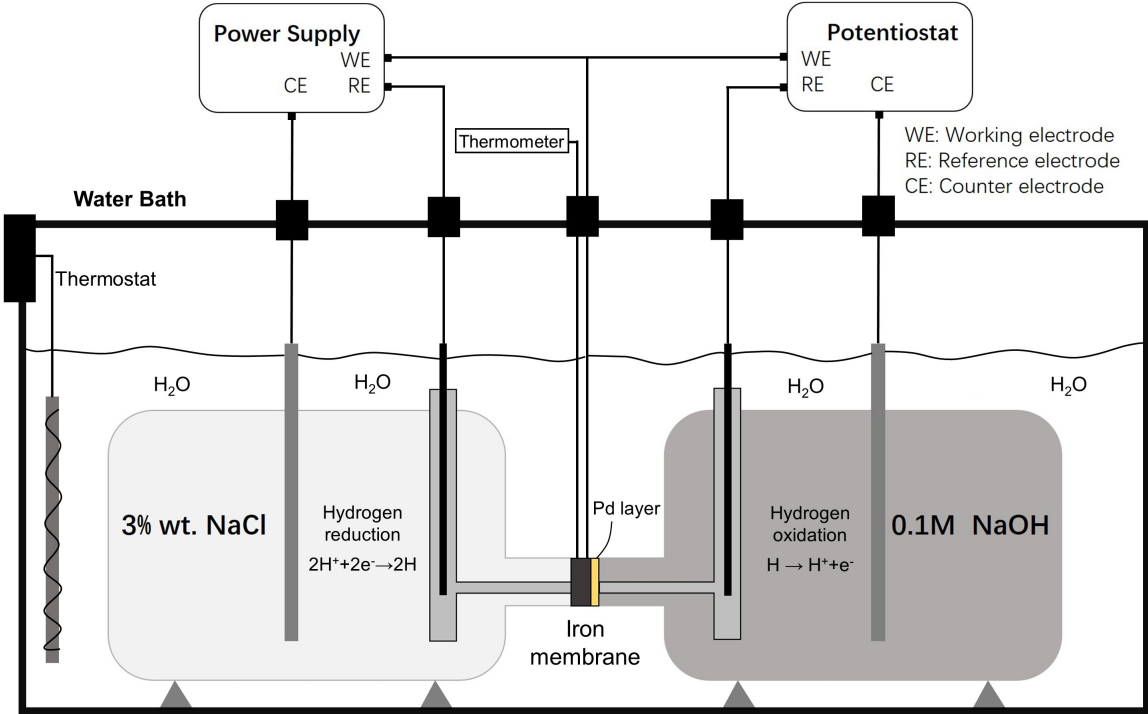


Figure 1: Schematic of the electrochemical permeation testing configuration used in this work. The permeation setup is placed into a water bath to conduct high-temperature experiments.

Prior to conducting each permeation experiment, a thin layer of Pd (approximately 50-nm thick) was electroplated onto the specimen surface facing the oxidation side of the double-cell. Electroplating was completed by applying a current density of 1 mA/cm<sup>2</sup> to the specimen for approximately 5 minutes while it was immersed in a commercial solution that contained 2 g/L of Pd. The Pd layer is employed for two reasons (Manolatos et al., 1995): (1) to enhance the hydrogen oxidation reaction kinetics so as to minimize the hydrogen concentration at the sample surface in the oxidation cell, and (2) to avoid the oxidation of iron, which would obfuscate the true hydrogen permeation current. Once plated, the specimen was inserted into the Devanathan-Stachurski double-cell and the open-circuit potential (OCP) of the sample membrane was monitored on the oxidation side of the cell for 1 hour. Upon completing this 1 hour hold, the oxidation side of the membrane was then polarized to the final potential recorded during the OCP measurement (typically between -40 and -60 mV<sub>SCE</sub>). The permeation current density was then allowed to stabilize to a value less than 0.1 to 0.2 μA/cm<sup>2</sup> before the galvanostatic cathodic charging was started on the reduction side of the double-cell.

### *2.2.1. Determination of the diffusion coefficient*

A representative hydrogen permeation transient versus time relationship that would be generated during an electrochemical permeation experiment is provided in Fig. 2. From these data, the hydrogen diffusivity can be calculated using three different methods (Turnbull et al., 1989): (i) the breakthrough time method, (ii) the lag time method, and (iii) by fitting the permeation transient to an approximate solution of Fick's law (Crank, 1979). The last case involves fitting the entire permeation transient, while the first two approaches use closed-form solutions to relate the time required to reach specific fractions of the steady state permeation current density,  $J_{\infty}$ , to the hydrogen diffusion coefficient  $D$ . In each case, it is assumed that the hydrogen subsurface concentration is a constant finite value at the entry side and zero at the exit side of the membrane.

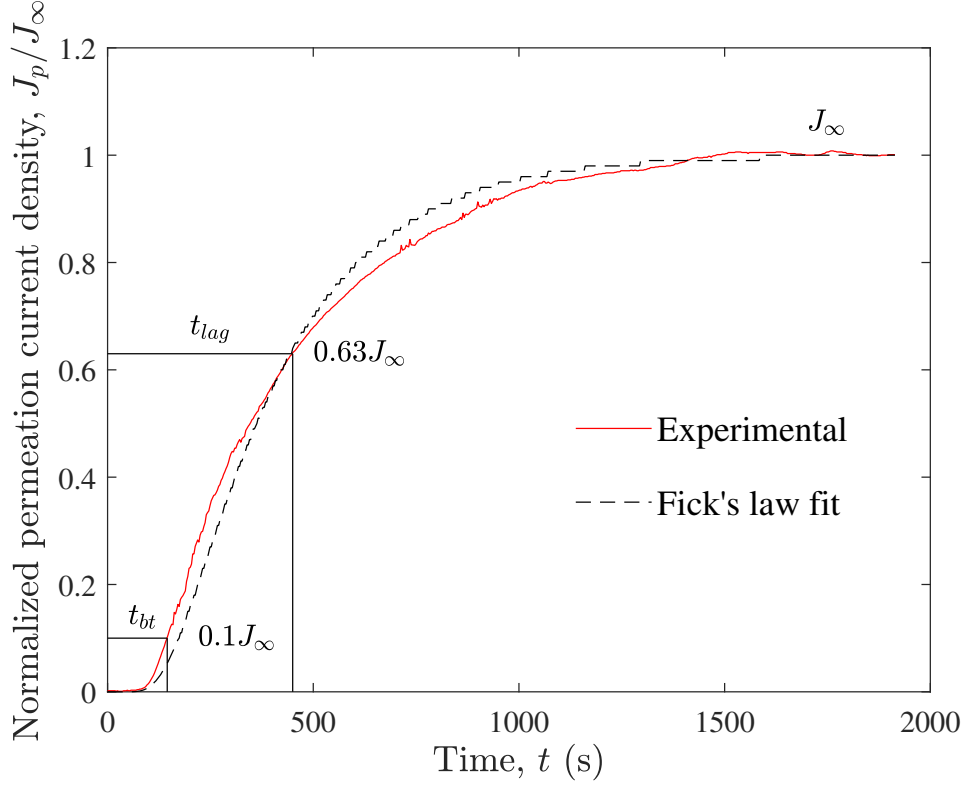


Figure 2: Typical rise permeation transient, with the three main methods used to determine the diffusivity superimposed on the experimental results.

Regarding the first method, the breakthrough time,  $t_{bt}$ , is identified as the time required for  $J_p$  to reach 10% of  $J_\infty$  (*i.e.*,  $J_p/J_\infty=0.1$ ) and is nominally considered to be the time required for the first hydrogen atoms to permeate completely through the membrane. Assuming a membrane geometry of thickness  $L$ , the hydrogen diffusivity,  $D_{bt}$ , can then be analytically determined for a given  $t_{bt}$  using:

$$D_{bt} = \frac{L^2}{15.3t_{bt}} \quad (1)$$

For the lag time method, the hydrogen diffusivity,  $D_{lag}$ , is obtained in a similar manner as the breakthrough approach. Specifically, the lag time,  $t_{lag}$ , is identified as the time required to achieve a  $J_p$  that is 63% of  $J_\infty$ , which is then related to  $D_{lag}$  using:

$$D_{lag} = \frac{L^2}{6t_{lag}} \quad (2)$$

Lastly, the entire permeation transient as a function of time can be fit *via* least-squares regression to an approximate solution to Fick’s second law obtained from either a Laplace or Fourier transform (Crank, 1979), assuming 1-D diffusion. For this approach, the hydrogen diffusivity,  $D_{lpc}$ , is used as the sole fitting parameter to achieve the best fit between the experiment and predicted  $J_p/J_\infty$  versus time relationship, with the predicted relationship determined from:

$$\frac{J_p}{J_\infty} = \frac{2}{\pi^{1/2}} \frac{L}{(D_{lpc}t)^{1/2}} \exp\left(-\frac{L^2}{4D_{lpc}t}\right) \quad (3)$$

The hydrogen diffusion coefficients measured with these three techniques were compared and differences discussed.

### 2.3. Hydrogen charging

Specimens were electrochemically precharged with hydrogen using a Gamry 1010B potentiostat operated in galvanostatic mode to maintain a constant cathodic current density,  $J_c$ . All charging experiments were performed with the specimen fully immersed in 3 wt. % NaCl solution and referenced to a Pt electrode; a schematic of the hydrogen charging setup is shown in Fig. 3. Based on previously reported diffusivities for cold-rolled Fe ( $D \approx 8 \times 10^{-11}$  m<sup>2</sup>/s; Van den Eeckhout et al., 2017), all specimens were precharged for 3 hours to obtain a nominally uniform hydrogen concentration across the plate thickness.

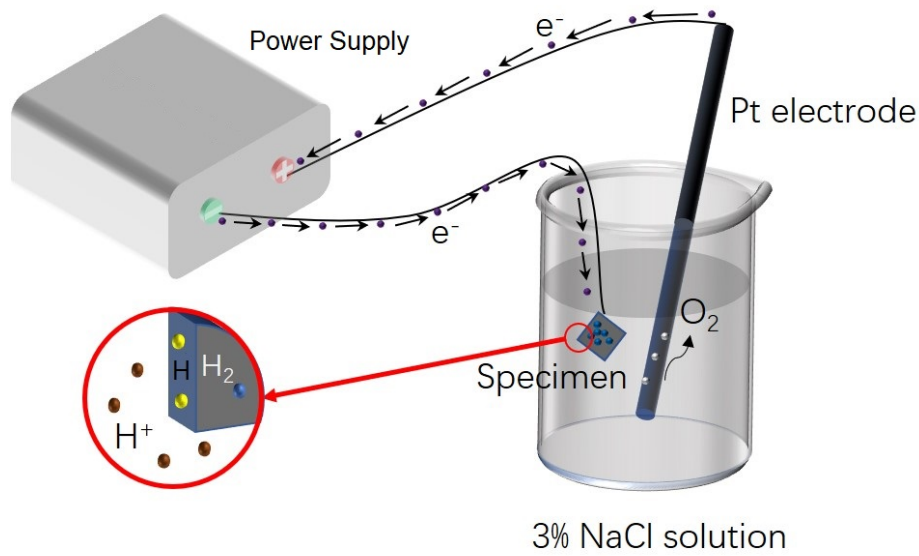


Figure 3: Schematic of the electrochemical hydrogen charging setup.

#### 2.4. TDS measurements

All desorption-based experiments were completed using a dedicated thermal desorption spectroscopy (TDS) system capable of achieving heat rates as fast as 60°C/min (3600 K/h). The system consisted of a dedicated analysis chamber, which was maintained at a vacuum pressure of  $10^{-9}$  mbar using a turbomolecular pump, and a small sample loading chamber designed to minimize the time required to reach vacuum levels comparable to the analysis chamber. Hydrogen content measurements were made using a regularly calibrated Hiden Analytical RC PIC quadrupole mass spectrometer, which had a detection resolution of  $4.4 \times 10^{-6}$  wppm/s. For each thermal desorption experiment, the sample was electrochemically pre-charged with hydrogen according to the process described in Section 2.3. Upon completion of the cathodic charging, the sample was rinsed with acetone and then distilled water, carefully dried with warm air, and then loaded into the transfer chamber of the TDS. The transfer system was then evacuated to approximately  $10^{-7}$  mbar. After the transfer from the loading chamber was complete, the specimen was placed onto an aluminium nitride (AlN) sheet in direct contact with the controllable, 2.5 kW heating stage. Four ceramic rods were then

extended to press the sample against the AlN sheet, thereby maximizing conduction as well as ensuring homogeneous heating of the entire specimen. Once the specimen had been sufficiently fixed against the AlN plate, the desorption experiment was initiated using a pre-programmed temperature versus time sequence. The typical elapsed time between the completion of cathodic charging and the beginning of the thermal desorption experiment was 30 minutes. A schematic illustrating this experimental setup is shown in Fig. 4.

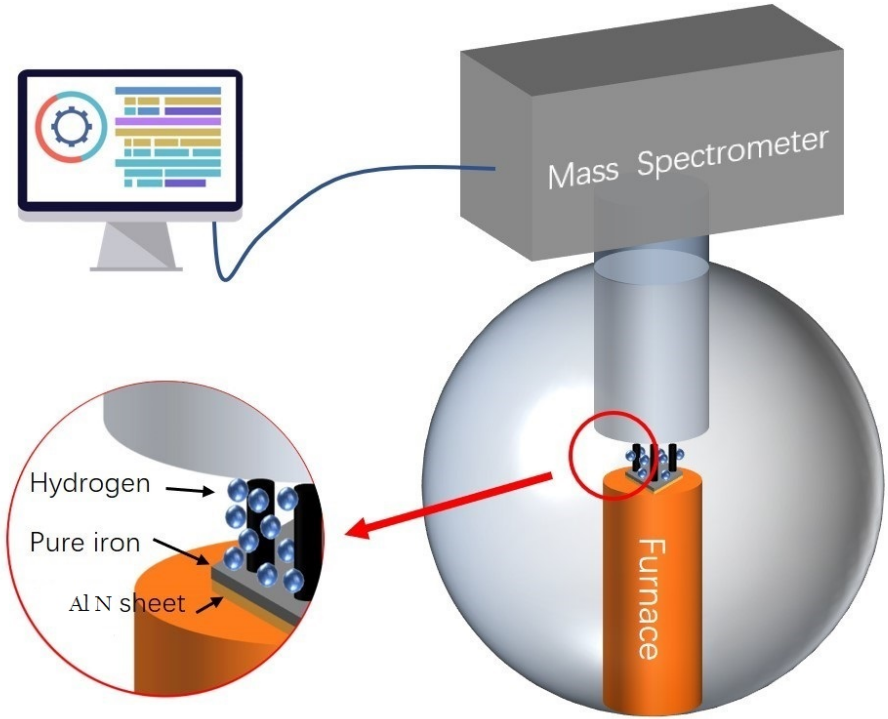


Figure 4: Schematic representation of the thermal desorption spectrometer during a measurement, including a detailed sketch of sample fixation system used to maximize the heating response.

Two types of thermal desorption experiments were performed in the current study to assess the hydrogen diffusivity of cold-rolled pure iron, as described in the following sections.

#### 2.4.1. Desorbed hydrogen tests

A series of 10 mm x 10 mm x 1 mm specimens were cathodically pre-charged in 3 wt. % NaCl solution using a current density of 5 mA/cm<sup>2</sup> during a charging time of 3 hours. After charging, the samples were then allowed to rest at ambient temperature ( $\approx 22^\circ\text{C}$ ) in laboratory air for times (which included the TDS pump-down time) ranging from 0.5 to 48 hours. Each sample was then heated from 25 to 850°C at a rate of 30°C/min and the total remaining hydrogen content was calculated *via* integration of the obtained thermal desorption spectra. The hydrogen diffusivity at ambient temperature,  $D_{des}$ , can then be determined by comparing the experimental hydrogen content versus desorption time relationship to that predicted by published analytical solutions for 1-D diffusion in a plate geometry of half-thickness  $L$ , such as (Crank, 1979):

$$\frac{C - C_0}{C_1 - C_0} = 1 - \frac{4}{\pi} \sum_{n=0}^{\infty} \frac{(-1)^n}{2n + 1} \exp \left\{ -D_{des}(2n + 1)^2 \pi^2 t / 4L^2 \right\} \cos \frac{(2n + 1)\pi x}{2L} \quad (4)$$

where  $C$  is the hydrogen concentration at position  $x$  after desorption time  $t$ ,  $C_0$  is the initial uniformly distributed hydrogen concentration at  $t = 0$  seconds, and  $C_1$  is the surface hydrogen concentration. A Matlab script was used to iteratively increment  $C_0$  and  $D_{des}$  to obtain the optimal fit between the average concentration across the simulated specimen thickness and the measured remaining total hydrogen content for each desorption time. Note that there are several critical assumptions in this analysis. First, given that the desorbed hydrogen content contains the trapped hydrogen, which is unlikely to desorb at ambient temperature, the total hydrogen content was found to asymptotically approach a lower-bound plateau value at long desorption times. This was phenomenologically captured in this simulation by considering  $C_1$  to be the trapped hydrogen concentration which, based on the desorption experiment results (see Fig. 7), was set to a constant value of 0.75 weight parts per million (wppm). Second, a constant specimen thickness of 1 mm was assumed for all simulations. Lastly, an initially uniform concentration is assumed, in accordance with the boundary conditions used for the derivation of Eq. (4) (Crank, 1979).

### 2.4.2. Isothermal TDS tests

Isothermal desorption experiments were performed at 22, 40, 60, and 80°C on a series of 10 mm x 10 mm x 1 mm specimens that were each cathodically pre-charged in 3 wt. % NaCl solution using a current density of 5 mA/cm<sup>2</sup> during charging time of 3 hours. Duplicate experiments were also performed at 22°C and 80°C. These isothermal experiments are nominally similar to typical programmed-temperature desorption (Verbeke, 2012), but hydrogen egress is monitored under a fixed temperature, as opposed to ramping the temperature versus time profile. For all tested temperatures greater than 22°C, the time required to stabilize the sample at the test temperature varied from 140 to 180 seconds.

Given the isothermal nature of these experiments, it is straightforward to determine the hydrogen diffusivity from the desorbed hydrogen content versus time profile using numerical analysis approaches (e.g., finite differences or finite element). In this work, we chose to use finite element modelling to determine the hydrogen diffusivity from the isothermal TDS tests. The magnitude of the hydrogen diffusion coefficient  $D$  can be determined by fitting the experimental desorption curve with the output of a 1D finite element (FE) simulation of hydrogen transport. Specifically, diffusion is governed by Fick's second law, which in a one-dimensional form reads:

$$\frac{\partial C}{\partial t} = D \frac{\partial^2 C}{\partial x^2} \quad (5)$$

where  $C$  is the diffusible hydrogen concentration. One must also define an initial condition ( $C = C_0$  at  $t = 0$ ) and suitable boundary conditions ( $C = 0$  at  $x = \pm L/2$ ). The simulations were then completed as follows. First, the hydrogen egress during experiments associated with the resting time required for the chamber pump-down (30 min.) and subsequent heating time to reach the targeted temperature,  $T_{iso}$ , was simulated by assuming the sample was held at room temperature ( $T = 22^\circ\text{C}$ ) for the entire rest and heating duration. Then, upon completing this initial hold time, the temperature in the simulation was instantly increased to  $T_{iso}$  and then held constant for the duration of the

simulation. The diffusivity used in the initial resting step of the simulations was determined by first fitting the experimentally-measured desorbed hydrogen content versus time data obtained at 22°C *via* iteratively changing the  $C_0$  and  $D$  values. Once this value was known, the best  $D$  at  $T = 22^\circ\text{C}$  was then applied for the resting period for the higher temperature experiments, with  $C_0$  and  $D$  then adjusted to fit the observed desorption data for each respective  $T_{iso}$ . A sensitivity analysis revealed the existence of a unique pair of  $C_0$  and  $D$  values that yielded the best fit of the experimental curve for each temperature. Critically, while the simulation results were found to be minorly affected by changes in  $C_0$ , they were strongly sensitive to subtle changes in  $D$ , thereby indicating the uniqueness of the best fit  $D_{iso}$  for each temperature.

### 3. Results

#### 3.1. Influence of the charging current

First, it is necessary to determine the cathodic current density,  $J_c$ , to be employed for subsequent hydrogen precharging and permeation experiments, as well as to establish a general relationship between applied current density and total hydrogen content for cold-rolled Fe. Towards this end, specimens were charged at seven different current densities ranging from 0.5 to 13 mA/cm<sup>2</sup>. The total hydrogen content was then calculated *via* integration of the TDS spectra collected for each specimen over the temperature range of 25 to 850°C. A total of 31 specimens were evaluated: 1 specimen at 0.5 mA/cm<sup>2</sup>, 1 specimen at 1 mA/cm<sup>2</sup>, 1 specimen at 3 mA/cm<sup>2</sup>, 22 specimens at 5 mA/cm<sup>2</sup>, 1 specimen at 7 mA/cm<sup>2</sup>, 3 specimens at 10 mA/cm<sup>2</sup>, and 2 specimens at 13 mA/cm<sup>2</sup>. The measured total hydrogen content  $C$  as a function of  $J_c$  is shown in Fig. 5. For the current densities where multiple experiments were performed, the average measured concentration is plotted, with the error bars representing the calculated standard deviation. These data were then fit to a power law function, yielding the following relationship:  $C = 1.342J_c^{0.3102}$ , as indicated by the solid line in Fig. 5. The 95% prediction bands, which represent the upper and lower bounds between which

there is 95% confidence the fitted function will reside, are represented by dashed lines in Fig. 5.

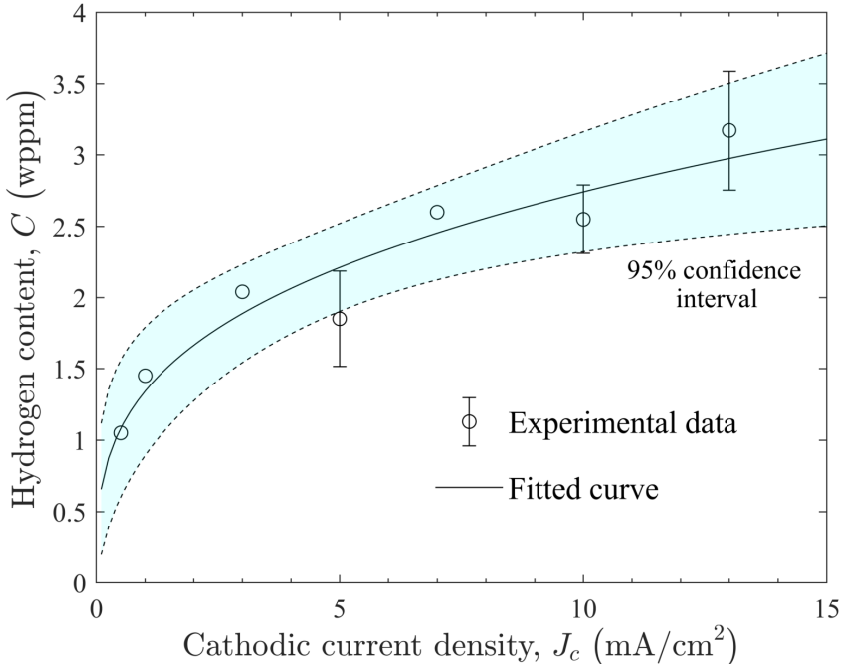


Figure 5: Evolution of the hydrogen concentration with the current density and prediction model.

Examination of Fig. 5 reveals four observations. First, the total hydrogen content exhibits an initially rapid increase with increasing  $J_c$  up to 3 mA/cm<sup>2</sup>, followed by a more gradual increase over the remaining range of evaluated current densities. This asymptotic-like behavior at the relatively low hydrogen contents of between 3 to 3.5 wppm is consistent with the generally low hydrogen solubility of  $\alpha$ -iron (Choo et al., 1981). Second, regarding the solubility of hydrogen in pure Fe, the literature establishes that it is on the order of 1 wppm (Choo et al., 1981), which is lower than the values reported here. However, it should be noted that the evaluated pure Fe was cold rolled down to its final thickness of 1 mm. As such, an increase in solubility is expected due to the multiplication of defects, which will act as trap sites and increase the total hydrogen concentration (Kiuchi and McLellan, 1983; Oriani, 1970). Third, as demonstrated by both the upper and lower bounds of the prediction interval and the error bars calcu-

lated from duplicate experiments, the dataset is well described by the fitted power law equation. Lastly, the observed relative scatter of the data, especially for the 5 mA/cm<sup>2</sup> condition where 22 specimens were evaluated, is in line with expectations from other electrochemical charging studies of hydrogen content (Ai et al., 2013; Rincon Troconis et al., 2017; Harris et al., 2021b) and suggests reasonable repeatability amongst the duplicate specimens.

### 3.2. Permeation tests

The permeation curves obtained for duplicate experiments on cold-rolled pure Fe at 22, 40, and 67°C, along with their corresponding fits to Eq. (3), are shown in Fig. 6. For each experiment, the steady state permeation current density ( $J_\infty$ ), breakthrough time ( $t_{bt}$ ), and lag time ( $t_{lag}$ ) are documented in Table 1. The calculated hydrogen diffusivities using the three approaches described in Section 2.2 are also noted. First, considering the results at 22°C, the diffusivity is found to vary between 4 and  $7.4 \times 10^{-11}$  m<sup>2</sup>/s across the three employed methods, which is broadly consistent with reported hydrogen diffusivities for cold-rolled pure Fe (Van den Eeckhout et al., 2017). Second, both the slope of the permeation transient and the magnitude of  $J_\infty$  systematically increase with temperature, as expected from literature results (Addach et al., 2005; Barrer, 1940). This implies an increase of the hydrogen diffusivity with temperature, as can be seen in Table 1, across all the methodologies employed. Third, it is important to note that the assumed diffusivity employed to estimate the time required for hydrogen precharging of the desorption experiments ( $D \approx 8 \times 10^{-11}$  m<sup>2</sup>/s; Van den Eeckhout et al., 2017) was a reasonable estimate. Critically, considering the calculated diffusivities for 22°C in Table 1, it is expected that the centerline of the 1-mm thick specimens used in the current study would indeed be nominally saturated after 3 hours; *i.e.*, reached between 98.20% and 99.95% of the surface hydrogen concentration, as per Eq. (4).

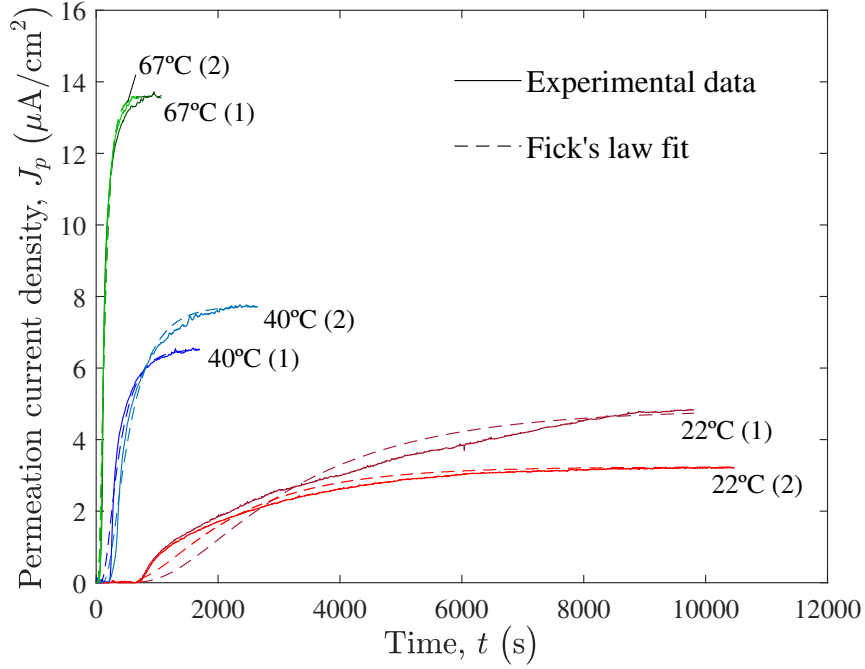


Figure 6: Permeation transients obtained in pure Fe at different temperatures, including a fit using Fick's law.

Table 1: Diffusivity values calculated from the permeation transients.

Test	$J_{\infty}$ ( $\mu\text{A}/\text{cm}^2$ )	$t_{bt}$ (s)	$D_{bt}$ ( $\text{m}^2/\text{s}$ )	$t_{lag}$ (s)	$D_{lag}$ ( $\text{m}^2/\text{s}$ )	$D_{lpc}$ ( $\text{m}^2/\text{s}$ )
22°C (1)	4.85	870	$7.36 \times 10^{-11}$	4110	$3.97 \times 10^{-11}$	$4.53 \times 10^{-11}$
22°C (2)	3.24	834	$6.78 \times 10^{-11}$	2596	$5.55 \times 10^{-11}$	$5.89 \times 10^{-11}$
40°C (1)	6.52	245	$2.21 \times 10^{-10}$	377	$3.66 \times 10^{-10}$	$3.31 \times 10^{-10}$
40°C (2)	7.73	315	$1.83 \times 10^{-10}$	570	$2.57 \times 10^{-10}$	$2.41 \times 10^{-10}$
67°C (1)	13.60	87	$6.22 \times 10^{-10}$	145	$9.52 \times 10^{-10}$	$8.52 \times 10^{-10}$
67°C (2)	13.56	80	$7.19 \times 10^{-10}$	151	$9.71 \times 10^{-10}$	$9.24 \times 10^{-10}$

Examination of the Laplace Fick's law fit for each experiment in Fig. 6 demonstrates that steady state conditions were attained in each experiment, as shown by the good agreement between the experimental and fitted curves. The exception is the 22°C (1)

case, where stabilisation of the permeation curve was not observed. Speculatively, the difficulty in reaching steady state for this experiment may be due either to surface effects taking place in the cathodic or anodic sides of the specimen (Kiuchi and McLellan, 1983; Addach et al., 2009) or to incomplete filling of the hydrogen traps (Kumnick and Johnson, 1974; Oriani, 1970). As such, it is likely that the reported diffusivities determined for this test are biased to slightly higher values. This situation exemplifies a primary limitation of electropermeation tests when assessing hydrogen diffusivity in metals as numerous variables can hinder the attainment of steady state, thereby obfuscating subsequent analysis efforts.

Comparing the calculated diffusivities for each method in Table 1, it is interesting to note that the lag time and the Laplace methods resulted in similar hydrogen diffusivities across all tested specimens, with the largest differences being less than 12%. Conversely, the diffusivities determined with the breakthrough method at 22°C were noticeably higher than those obtained with the lag time and Laplace methods, but then found to be lower in the case of the tests performed at higher temperatures. Speculatively, this behaviour could be explained in terms of the progressive loss of importance of trapping phenomena over lattice diffusion as the temperature is increased (Oriani, 1970). It is worth noting that the differences in diffusivity between the breakthrough and the lag time/Laplace methods increased to nearly 40% in some cases, which is greater than the scatter reported between duplicate experiments.

### *3.3. Desorption curve*

The results of the ‘rest time’-based approach to measuring hydrogen diffusivity *via* desorption methods is shown in Fig. 7. As expected, the total hydrogen concentration within the specimen exhibits an initially strong reduction with increasing rest time at ambient temperature, eventually leveling out at a nominal concentration of 0.75 wppm after approximately 10-15 hours. This initial steep reduction is consistent with the egress of the diffusible hydrogen concentration, while the observed plateau is indicative of the trapped hydrogen content. These data were then iteratively fit to Eq. (4), with

$C_0$  and  $D_{des}$  used as fitting parameters. The results of the best obtained fit are indicated by the red line in Fig. 7, which corresponded to  $C_0 = 3.0$  wppm and  $D_{des} = 1 \times 10^{-11}$  m<sup>2</sup>/s. Comparing this value to those obtained from the various permeation methods at 22°C (Table 1), it is clear that the ‘rest time’ desorption approach yields a tangibly lower diffusivity. Possible reasons for this decreased diffusivity will be enumerated in the Discussion section.

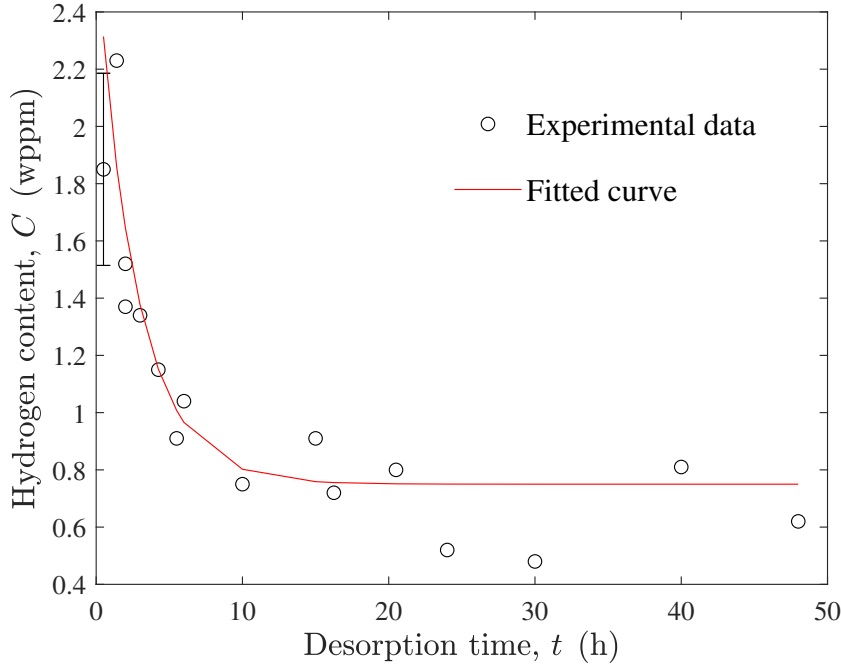


Figure 7: Desorption curve. Hydrogen concentration as a function of elapsed time in air at room temperature. The datapoint and error bars at 0.5 hours represent the average and standard deviation of the total content measured from 22 experiments.

### 3.4. Isothermal TDS tests

The measured desorption rate versus time profiles during isothermal desorption experiments at temperatures of 22, 40, 60 and 80°C are shown in Fig. 8. The initial slope of the desorption rate versus time relationship is noted to increase with increasing temperature, consistent with expectations for an increasing hydrogen diffusivity and with the behavior observed during the permeation experiments (Fig. 6). The best

fit to Fick's second law, determined from finite element (FE) simulations, is indicated by the corresponding dashed lines for each respective condition. For all cases, the FE calculations closely capture the experimentally observed initial slope, which is a strong function of the hydrogen diffusivity. The initial diffusible hydrogen concentration ( $C_0$ ) and diffusion coefficient ( $D_{iso}$ ) that yielded the best fit of the experimental curve with Fick's second law (FE model) are shown in Table 2. As expected, and in line with the permeation results, the calculated diffusivity exhibits a systematic increase with increasing temperature.

Finally, it is worth noting that very similar diffusion coefficients were obtained for the replicate tests performed at 22°C and 80°C, respectively. This is observed even though noticeable differences are seen in the fitted  $C_0$  values, though these variations in  $C_0$  lie within the scattering reported in Fig. 5. This excellent repeatability suggests this method - isothermal TDS tests combined with numerical fitting - is a robust approach for the determination of hydrogen diffusivities.

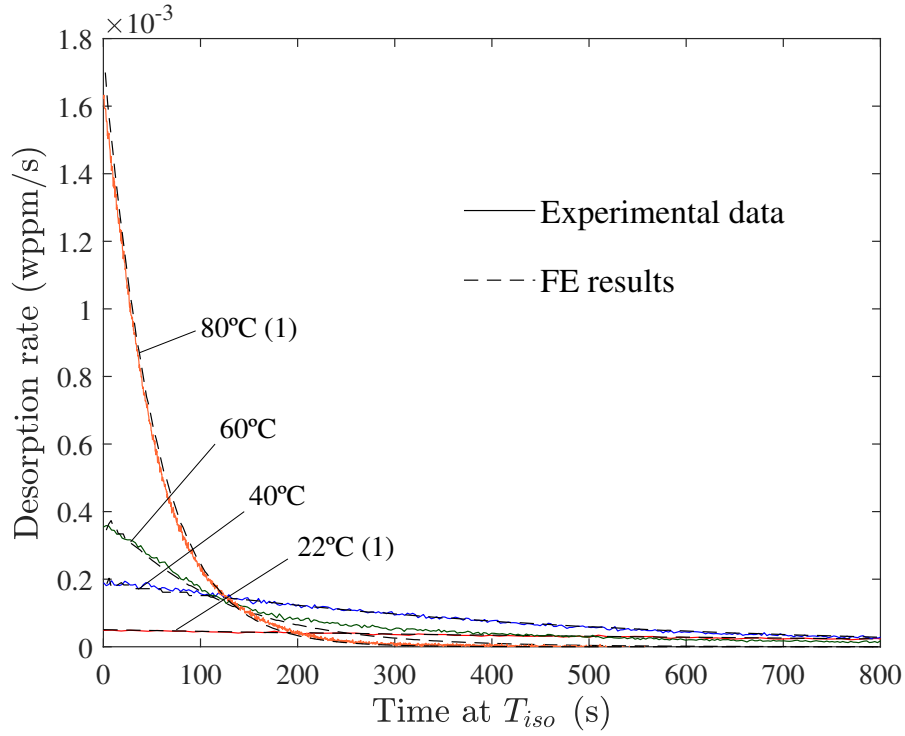


Figure 8: Isothermal TDS tests (solid lines) performed at different temperatures and results from the finite element analysis to estimate  $D$  (dashed lines).

Table 2: Initial diffusible hydrogen concentration,  $C_0$ , and diffusivity values,  $D_{iso}$ , estimated through FE modelling from isothermal TDS tests.

Test	$C_0$ (wppm)	$D_{iso}$ ( $m^2/s$ )
22°C (1)	0.27	$7.8 \times 10^{-11}$
22°C (2)	0.45	$7.5 \times 10^{-11}$
40°C	0.70	$2.0 \times 10^{-10}$
60°C	0.42	$7.0 \times 10^{-10}$
80°C (1)	0.68	$1.7 \times 10^{-9}$
80°C (2)	0.19	$1.3 \times 10^{-9}$

#### 4. Discussion

We proceed to compare and analyse the results obtained by the various permeation and desorption methods. The estimated diffusivities are shown versus the inverse of temperature in Fig. 9, using a log-linear plot. Here, the solid lines represent a fit of each respective dataset to the following Arrhenius expression:

$$D = D_0 \exp\left(\frac{-E_a}{RT}\right) \quad (6)$$

where  $D_0$  is the pre-exponential factor,  $E_a$  the activation energy for hydrogen diffusion, and  $R$  is the gas constant. The independent term of the linear regression is equal to  $\log(D_0)$  and  $E_a$  is obtained by multiplying the slope by  $R$ . The fitted values of  $D_0$  and  $E_a$  are shown in Table 3.

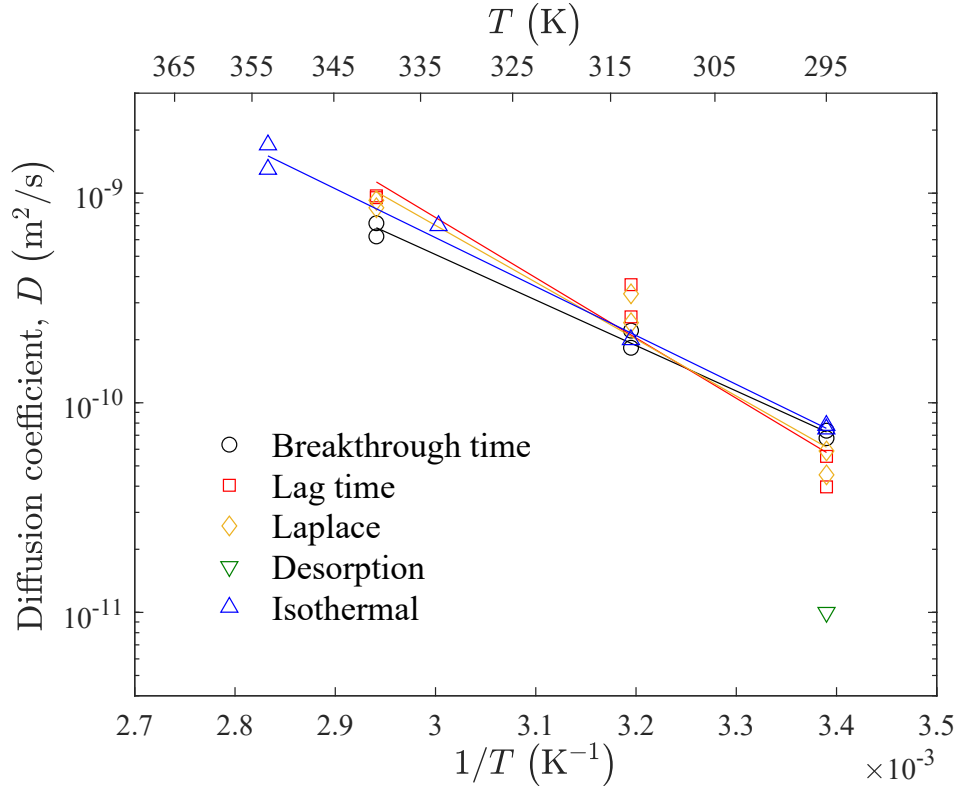


Figure 9: Estimated diffusivities versus the inverse of temperature for the various permeation and desorption methods investigated.

Table 3: Pre-exponential factor,  $D_0$ , and activation energy for hydrogen diffusion,  $E_a$ , as determined from permeation and isothermal desorption.

Method	$D_0$ (m <sup>2</sup> /s)	$E_a$ (kJ/mol)
Breakthrough time	$1.65 \times 10^{-3}$	41.5
Lag time	$3.22 \times 10^{-1}$	55.0
Laplace	$9.70 \times 10^{-2}$	51.9
Isothermal	$6.68 \times 10^{-3}$	44.9

Four observations can be made from these data. First, the desorption-based ‘rest time’ method yielded a significantly lower hydrogen diffusivity at 22°C (nearly five-fold) as compared to the other four approaches. Given that this approach is based on fitting the measured remaining hydrogen content as a function of outgassing time, it is speculated that variations in absorbed hydrogen concentration are likely responsible for the low observed diffusivity. As demonstrated by the error bars shown in Fig. 7 for the 22 duplicate measurements performed at 0.5 hours, test-to-test scatter in initially absorbed hydrogen content is non-negligible, which would introduce increased variability into this method relative to other approaches. Second, the isothermal desorption method yielded generally similar diffusivity values for a given temperature relative to the three permeation based approaches. Such agreement between the diffusivity values measured through both methods was not expected, as considerable differences between absorption-based and desorption-based measurements of diffusivity have been previously reported for elevated temperature (> 400°C)-based evolution experiments in pure iron (Carmichael et al., 1960). Third, examination of the spread in diffusivities at ambient temperature indicates a maximum of two-fold difference across the four best methods (permeation and isothermal desorption), which represents excellent agreement relative to the reported spread in ambient temperature diffusivity for pure Fe in the literature (Ono and Rosales, 1968; Kumnick and Johnson, 1974; Kiuchi and McLellan, 1983). Lastly, examination of the calculated  $E_a$  for the four approaches that were con-

ducted at multiple temperatures demonstrates that the isothermal desorption-based  $E_a$  sits in the middle of the three permeation-based approaches. Speculatively, it is likely that the agreement between these different methods would only increase if the isothermal desorption results were compared against the second permeation transient, which represents a scenario where the deep hydrogen traps are already filled.

As expected, the diffusion coefficients determined from the current experiments shown in Table 3 are significantly different from those measured in the literature for well-annealed pure Fe. For example, a thorough analysis of the existing diffusivity literature in well-annealed iron was performed by Kiuchi and McLellan, who suggested that hydrogen diffusion is best described by  $D_0 = 7.23 \times 10^{-8} \text{ m}^2/\text{s}$  and an activation energy  $E_a=5.69 \text{ kJ/mol}$  up to a temperature of  $80^\circ\text{C}$  (Kiuchi and McLellan, 1983). Considering the activation energy parameter, it is expected that the significantly increased dislocation density induced during the cold-rolling process will result in the widespread distribution of modestly strong hydrogen trap sites, thereby increasing the macroscale barrier for hydrogen diffusion (Oriani, 1970). For example, Choo and Lee (1983) observed a progressive increase in both  $D_0$  and  $E_a$  with the degree of cold rolling for pure iron. As such, the measured diffusivity is no longer controlled simply by lattice diffusion, but rather becomes dependent on the trapping behavior, resulting in diffusion being best described by an *effective diffusivity* (Oriani, 1970).

Given this expected departure from the behavior of annealed pure Fe, the current study’s results should be compared to the diffusivity versus temperature data reported from studies on cold-rolled Fe. This comparison is shown in Fig. 10 for six relevant studies (Addach et al., 2005; Choo and Lee, 1983; Drexler et al., 2020; Siegl et al., 2019; Van den Eeckhout et al., 2017; Li et al., 2014). The degree of cold rolling involved in each study has been included next to the corresponding data point in Fig. 10. As was discussed previously based on analyses conducted in the literature (Kiuchi and McLellan, 1983), literature data exhibits substantial scatter in measured diffusivity at

ambient temperature (300 K). Fig. 10 demonstrates that this large variability persists in cold-worked iron, as iron with similar degrees of cold work ( $\sim 50\%$ ) exhibits one order of magnitude differences in measured diffusivity. However, it is notable that the current results fall approximately in the middle of the observed scatter, suggesting general agreement with these prior data. Less literature data on cold-rolled iron is available at elevated temperatures, but the trend of the current results residing in the nominal middle of the scatter band appears to generally hold as the temperature is increased.

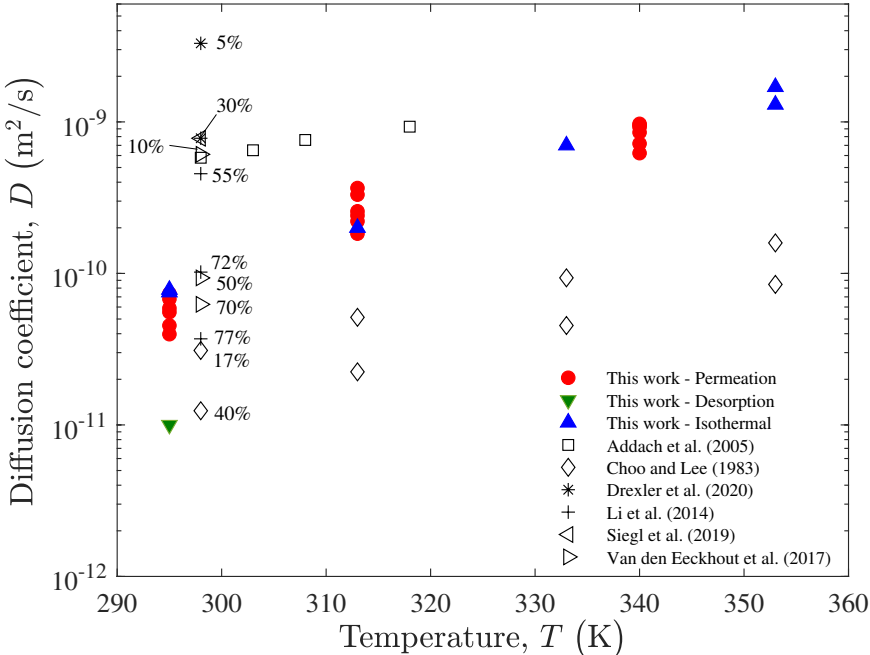


Figure 10: Measured and reported values of the diffusion coefficient of hydrogen in cold-rolled iron as a function of temperature. The degree of cold rolling is indicated; the data from the present work corresponds to a supplier-reported average degree of cold work of 50%.

Collectively, these comparisons with prior literature data and the reasonable agreement with the three different permeation-based approaches (Fig. 9 and Table 3) strongly support the viability of the employed isothermal desorption approach for assessing hydrogen diffusivity in cold-rolled Fe and other ‘fast’ diffusion alloy systems. Moreover, the efficacy of this method was demonstrated using a relatively thin mate-

rial form (1-mm thick sheet), indicating that the approach does not inherently require the large sample sizes employed in prior isothermal desorption-based studies (Yamabe et al., 2015). Given the large scatter band inherent to permeation-based measurements of the hydrogen diffusivity at low temperatures in pure Fe (Kiuchi and McLellan, 1983; Kumnick and Johnson, 1974), the use of alternative approaches should be considered and further investigated. In particular, it would be worthwhile to establish the degree of scatter in isothermal desorption-based diffusivity measurements of cold-rolled Fe. Moreover, as demonstrated by Fig. 10, the data density of hydrogen diffusivity measurements for cold-rolled Fe significantly decreases as the temperature is increased. The current study provides an initial set of reliable data for such elevated temperatures, but additional studies are needed to further populate the elevated temperature regime.

## 5. Conclusions

The hydrogen diffusivity for cold-rolled pure Fe was measured using both electrochemical permeation and thermal desorption-based techniques, offering an opportunity to compare these approaches. Based on these experiments, the following conclusions were made:

- Analysis of permeation data using the breakthrough time method, the lag time method, and a Laplace solution to the entire permeation transient yielded nominally similar hydrogen diffusivities across methodologies for each temperature (22°C, 40°C and 67°C). The hydrogen diffusivity values obtained at 22°C were found to be generally consistent with those reported in the literature for cold-rolled pure Fe.
- Comparison of two desorption-based approaches to calculating the hydrogen diffusion resulted in significantly different values, with differences between isothermal desorption and the rest time method being of almost an order of magnitude. This difference is speculatively attributed to the strong sensitivity of the rest time

method to the initial hydrogen concentration in each specimen, which was shown in Fig. 5 to exhibit substantial variation from test-to-test.

- Analysis of the Arrhenius relationships constructed from the hydrogen diffusivity versus temperature relationships demonstrates that the isothermal desorption approach yields nominally similar values of diffusion pre-exponential factor ( $D_0$ ) and activation energy ( $E_a$ ) to the permeation breakthrough time method. Slight differences are observed when comparing the isothermal results to lag time and Laplace permeation approaches. However, a collective analysis suggests that isothermal desorption is generally consistent with the permeation results.
- Hydrogen diffusivity values reported in the literature as a function of temperature for cold-rolled Fe are in excellent agreement with those determined in the current study using permeation and isothermal desorption.
- The results of this study demonstrate the efficacy of the isothermal desorption technique for evaluating hydrogen diffusivity in thin-section specimens of ‘fast’ diffusing materials. Additional studies are needed to evaluate the experimental scatter of this approach relative to that observed for permeation-based experiments, but initial results suggest that isothermal desorption exhibits reduced levels of scatter.

## 6. Acknowledgements

Emilio Martínez-Pañeda acknowledges discussions with A. Díaz (University of Burgos). The authors acknowledge financial support from the EPSRC (grants EP/V04902X/1 and EP/V009680/1).

## References

Addach, H., Berçot, P., Rezrazi, M., Takadoum, J., 2009. Study of the electrochemical permeation of hydrogen in iron. *Corrosion Science* 51, 263–267.

- Addach, H., Berçot, P., Rezrazi, M., Wery, M., 2005. Hydrogen permeation in iron at different temperatures. *Materials Letters* 59, 1347–1351.
- Ai, J.H., Ha, H.M., Gangloff, R.P., Scully, J.R., 2013. Hydrogen diffusion and trapping in a precipitation-hardened nickel-copper-aluminum alloy Monel K-500 (UNS N05500). *Acta Materialia* 61, 3186–3199.
- Akhurst, K.N., Baker, T.J., 1981. The threshold stress intensity for hydrogen-induced crack growth. *Metallurgical Transactions A* 12, 1059–1070.
- Barnoush, A., Vehoff, H., 2010. Recent developments in the study of hydrogen embrittlement: Hydrogen effect on dislocation nucleation. *Acta Materialia* 58, 5274–5285.
- Barrer, R.M., 1940. Stationary and non-stationary states of flow of hydrogen in palladium and iron. *Transactions of the Faraday Society* 36, 1235–1248.
- Bhadeshia, H.K.D.H., 2016. Prevention of Hydrogen Embrittlement in Steels. *ISIJ International* 56, 24–36.
- Boes, N., Züchner, H., 1976. Electrochemical methods for studying diffusion, permeation and solubility of hydrogen in metals. *Journal of The Less-Common Metals* 49, 223–240.
- Carmichael, D., Hornaday, J., Morris, A., Parlee, N., 1960. The absorption and effusion of hydrogen in alpha iron. *Transactions of the Metallurgical Society of AIME* 218, 826–832.
- Carvalho, J.P., Vilar, E.O., Araújo, B.A., 2017. A critical review and experimental analysis of the equation recommended by ASTM G148-97 and ISO 17081: 2004 for the calculation of the hydrogen diffusivity in metals and alloys. *International Journal of Hydrogen Energy* 42, 681–688.
- Choi, J.Y., 1970. Diffusion of hydrogen in iron. *Metallurgical Transactions* 1, 911–919.

- Choo, W.Y., Lee, J.Y., 1982. Thermal Analysis of Trapped Hydrogen in Pure Iron. *Metallurgical Transactions A* 13, 423–427.
- Choo, W.Y., Lee, J.Y., 1983. Effect of cold working on the hydrogen trapping phenomena in pure iron. *Metallurgical Transactions A* 14, 1299–1305.
- Choo, W.Y., Lee, J.Y., Cho, C.G., Hwang, S.H., 1981. Hydrogen solubility in pure iron and effects of alloying elements on the solubility in the temperature range 20 to 500° C. *Journal of Materials Science* 16, 1285–1292.
- Crank, J., 1979. *The mathematics of diffusion*. Oxford University Press, Oxford.
- DeLuccia, J., Berman, D., 1981. An Electrochemical Technique to Measure Diffusible Hydrogen in Metals (Barnacle Electrode), in: Mansfeld, F., Bertocci, U. (Eds.), *Electrochemical Corrosion Testing, ASTM STP 727*, American Society for Testing and Materials. pp. 256–273.
- Depover, T., Verbeken, K., 2021. Hydrogen diffusion in metals: a topic requiring specific attention from the experimentalist, in: Van der Voorde, M. (Ed.), *Hydrogen Storage for Sustainability, Vol. II*. Walter de Gruyter GmbH, Berlin. chapter 6, pp. 247–280.
- Díaz, A., Cuesta, I.I., Martínez-Pañeda, E., Alegre, J.M., 2020a. Analysis of hydrogen permeation tests considering two different modelling approaches for grain boundary trapping in iron. *International Journal of Fracture* 223, 17–35.
- Díaz, A., Cuesta, I.I., Martínez-Pañeda, E., Alegre, J.M., 2020b. Influence of charging conditions on simulated temperature-programmed desorption for hydrogen in metals. *International Journal of Hydrogen Energy* 45, 23704–23720.
- Díaz, A., Zafra, A., Martínez-Pañeda, E., Alegre, J.M., Belzunce, J., Cuesta, I.I., 2020c. Simulation of hydrogen permeation through pure iron for trapping and surface phenomena characterisation. *Theoretical and Applied Fracture Mechanics* 110, 102818.

- Djukic, M.B., Bakic, G.M., Sijacki Zeravcic, V., Sedmak, A., Rajcic, B., 2019. The synergistic action and interplay of hydrogen embrittlement mechanisms in steels and iron: Localized plasticity and decohesion. *Engineering Fracture Mechanics* 216, 106528.
- Drexler, A., Siegl, W., Ecker, W., Tkadletz, M., Klösch, G., Schnideritsch, H., Mori, G., Svoboda, J., Fischer, F.D., 2020. Cycled hydrogen permeation through Armco iron – A joint experimental and modeling approach. *Corrosion Science* 176.
- Fernández-Sousa, R., Betegón, C., Martínez-Pañeda, E., 2020. Analysis of the influence of microstructural traps on hydrogen assisted fatigue. *Acta Materialia* 199, 253–263.
- Galindo-Nava, E.I., Basha, B.I., Rivera-Díaz-del Castillo, P.E., 2017. Hydrogen transport in metals: Integration of permeation, thermal desorption and degassing. *Journal of Materials Science and Technology* 33, 1433–1447.
- Gangloff, R.P., 2003. Hydrogen-assisted Cracking, in: Milne, I., Ritchie, R., Karimhaloo, B. (Eds.), *Comprehensive Structural Integrity Vol. 6*. Elsevier Science, New York, NY, pp. 31–101.
- Gangloff, R.P., 2008. Critical Issues in Hydrogen Assisted Cracking of Structural Alloys, in: Shipilov, S.A., Jones, R.H., Olive, J.M., Rebak, R. (Eds.), *Environment-Induced Cracking of Materials Vol. 1*. Elsevier Science, New York, pp. 141–165.
- Gangloff, R.P., 2016. Probabilistic fracture mechanics simulation of stress corrosion cracking using accelerated laboratory testing and multi-scale modeling. *Corrosion* 72, 862–880.
- Gangloff, R.P., 2017. H-enhanced deformation and fracture in the crack tip process zone, in: Somerday, B.P., Sofronis, P. (Eds.), *Materials Performance in Hydrogen Environments: Proceedings of the 2016 International Hydrogen Conference*, ASME Press, Jackson Lake. pp. 1–35.
- Gangloff, R.P., Somerday, B.P., 2012. *Gaseous Hydrogen Embrittlement of Materials in Energy Technologies*. Woodhead Publishing Limited, Cambridge.

- Gerberich, W.W., 2012. Modeling hydrogen induced damage mechanisms in metals, in: Gangloff, R.P., Somerday, B.P. (Eds.), *Gaseous Hydrogen Embrittlement of Materials in Energy Technologies Vol. II*. Woodhead Publishing, pp. 209–246.
- Gonzalez, O., 1969. The measurement of hydrogen permeation in alpha iron: an analysis of experiments. *Transactions of the Metallurgical Society of AIME* 245, 607–612.
- Hafsi, Z., Elaoud, S., Mishra, M., 2019. A computational modelling of natural gas flow in looped network: Effect of upstream hydrogen injection on the structural integrity of gas pipelines. *Journal of Natural Gas Science and Engineering* 64, 107–117.
- Harris, Z.D., Bhattacharyya, J.J., Ronevich, J.A., Agnew, S.R., Burns, J.T., 2020. The combined effects of hydrogen and aging condition on the deformation and fracture behavior of a precipitation-hardened nickel-base superalloy. *Acta Materialia* 186, 616–630.
- Harris, Z.D., Dubas, E.M., Popernack, A.S., Somerday, B.P., Burns, J.T., 2021a. Elucidating the loading rate dependence of hydrogen environment-assisted cracking in a Ni-Cu superalloy. *Theoretical and Applied Fracture Mechanics* 111, 102846.
- Harris, Z.D., Guiseva, K., Scully, J.R., Burns, J.T., 2021b. On the hydrogen environment-assisted cracking resistance of a compositionally complex Co-Ni-Cr-Fe-Mo-Ti alloy. *Materials Science and Engineering A* 802, 140601.
- Harris, Z.D., Lawrence, S.K., Medlin, D.L., Guetard, G., Burns, J.T., Somerday, B.P., 2018. Elucidating the contribution of mobile hydrogen-deformation interactions to hydrogen-induced intergranular cracking in polycrystalline nickel. *Acta Materialia* 158, 180–192.
- Ishaq, H., Dincer, I., 2020. A comprehensive study on using new hydrogen-natural gas and ammonia-natural gas blends for better performance. *Journal of Natural Gas Science and Engineering* 81.

- Johnson, H.H., 1988. Hydrogen in Iron. *Metallurgical Transactions A* 19A, 2371–2387.
- Johnson, W.H., 1875. On Some Remarkable Changes Produced in Iron and Steel by the Action of Hydrogen and Acids. *Proceedings of the Royal Society of London* 23, 168–179.
- Kiuchi, K., McLellan, R.B., 1983. The solubility and diffusivity of hydrogen in well-annealed and deformed iron. *Acta Metallurgica* 31, 961–984.
- Kristensen, P.K., Niordson, C.F., Martínez-Pañeda, E., 2020. A phase field model for elastic-gradient-plastic solids undergoing hydrogen embrittlement. *Journal of the Mechanics and Physics of Solids* 143, 104093.
- Kunnick, A.J., Johnson, H.H., 1974. Hydrogen transport through annealed and deformed Armco iron. *Metallurgical Transactions* 5, 1199–1206.
- Lawrence, S.K., Yagodzinsky, Y., Hänninen, H., Korhonen, E., Tuomisto, F., Harris, Z.D., Somerday, B.P., 2017. Effects of grain size and deformation temperature on hydrogen-enhanced vacancy formation in Ni alloys. *Acta Materialia* 128, 218–226.
- Lawrenz, D.A., Mitchell, J., 2006. Thermal Evolution Methods for Carbon, Sulfur, Oxygen, Nitrogen and Hydrogen in Iron and Steel Analysis, in: *Encyclopedia of Analytical Chemistry: Applications, Theory, and Instrumentation*. John Wiley & Sons, Ltd, Chichester, UK.
- Lee, J.Y., Lee, J.L., 1987. A trapping theory of hydrogen in pure iron. *Philosophical Magazine A: Physics of Condensed Matter, Structure, Defects and Mechanical Properties* 56, 293–309.
- Li, Y., Cai, L., Liu, G., Ma, L., 2014. Effect of cold-rolled thickness reduction degree on characteristics of hydrogen diffusion in silicon steel. *International Journal of Corrosion* 2014.

- Manolatos, P., Jerome, M., Galland, J., 1995. Necessity of a palladium coating to ensure hydrogen oxidation during electrochemical permeation measurements on iron. *Electrochimica Acta* 40, 867–871.
- Martínez-Pañeda, E., Díaz, A., Wright, L., Turnbull, A., 2020. Generalised boundary conditions for hydrogen transport at crack tips. *Corrosion Science* 173, 108698.
- Martínez-Pañeda, E., Golahmar, A., Niordson, C.F., 2018. A phase field formulation for hydrogen assisted cracking. *Computer Methods in Applied Mechanics and Engineering* 342, 742–761.
- Martínez-Pañeda, E., Niordson, C.F., Gangloff, R.P., 2016. Strain gradient plasticity-based modeling of hydrogen environment assisted cracking. *Acta Materialia* 117, 321–332.
- Matsuo, T., Yamabe, J., Furukawa, H., Seki, K., Shimizu, K., Watanabe, S., Matsuoka, S., 2014. Development of New Strain Gage for High-Pressure Hydrogen Gas Use. *Experimental Mechanics* 54, 431–442.
- Melaina, M., Antonia, O., Penev, M., 2013. NREL/TP-5600-51995: Blending hydrogen into natural gas pipelines networks: a review of key issues. Technical Report. National Renewable Energy Laboratory. Golden, CO.
- Meng, B., Gu, C., Zhang, L., Zhou, C., Li, X., Zhao, Y., Zheng, J., Chen, X., Han, Y., 2017. Hydrogen effects on X80 pipeline steel in high-pressure natural gas/hydrogen mixtures. *International Journal of Hydrogen Energy* 42, 7404–7412.
- Mine, Y., Narazaki, C., Murakami, K., Matsuoka, S., Murakami, Y., 2009. Hydrogen transport in solution-treated and pre-strained austenitic stainless steels and its role in hydrogen-enhanced fatigue crack growth. *International Journal of Hydrogen Energy* 34, 1097–1107.
- Nagao, A., Dadfarnia, M., Somerday, B.P., Sofronis, P., Ritchie, R.O., 2018. Hydrogen-enhanced-plasticity mediated decohesion for hydrogen-induced intergranular and

- “quasi-cleavage” fracture of lath martensitic steels. *Journal of the Mechanics and Physics of Solids* 112, 403–430.
- Nagumo, M., Takai, K., 2019. The predominant role of strain-induced vacancies in hydrogen embrittlement of steels: Overview. *Acta Materialia* 165, 722–733.
- Nelson, H., Stein, J., 1973. NASA TN D-7265: Gas-phase hydrogen permeation through alpha iron, 4130 steel, and 304 stainless steel from less than 100°C to near 600°C. Technical Report. Ames Research Center. Moffat Field, CA.
- Nguyen, T.T., Park, J.S., Kim, W.S., Nahm, S.H., Beak, U.B., 2020. Environment hydrogen embrittlement of pipeline steel X70 under various gas mixture conditions with in situ small punch tests. *Materials Science and Engineering A* 781, 139114.
- Ono, K., Rosales, L., 1968. On the anomalous behavior of hydrogen in iron at lower temperatures. *Transactions of the Metallurgical Society of AIME* 242, 244–248.
- Oriani, R., 1970. The diffusion and trapping of hydrogen in steel. *Acta Metallurgica* 18, 147–157.
- Rincon Troconis, B.C., Harris, Z.D., Ha, H., Burns, J.T., Scully, J.R., 2017. The effect of heat-to-heat variations in metallurgy and hydrogen-metal interactions on the hydrogen embrittlement of Monel K-500. *Materials Science and Engineering A* 703, 533–550.
- Robertson, I.M., Sofronis, P., Nagao, A., Martin, M.L., Wang, S., Gross, D.W., Nygren, K.E., 2015. Hydrogen Embrittlement Understood. *Metallurgical and Materials Transactions B* 46, 1085–1103.
- Shang, J., Chen, W., Zheng, J., Hua, Z., Zhang, L., Zhou, C., Gu, C., 2020. Enhanced hydrogen embrittlement of low-carbon steel to natural gas/hydrogen mixtures. *Scripta Materialia* 189, 67–71.

- Shishvan, S.S., Csányi, G., Deshpande, V.S., 2020. Hydrogen induced fast-fracture. *Journal of the Mechanics and Physics of Solids* 134, 103740.
- Siegl, W., Ecker, W., Klarner, J., Kloesch, G., Mori, G., Drexler, A., Winter, G., Schnideritsch, H., 2019. Hydrogen trapping in heat treated and deformed Armco iron. *NACE - International Corrosion Conference Series 2019-March*.
- Stross, T., Tompkins, F.C., 1956. The diffusion coefficient of hydrogen in iron. *Proceedings of the Chemical Society of London* 1, 230–234.
- Subramanyan, P., 1981. Electrochemical Aspects of Hydrogen in Metals, in: Bockris, J., Conway, B., Yeager, E., White, R. (Eds.), *Comprehensive Treatise on Electrochemistry*, Plenum Press, New York. pp. 411–462.
- Turnbull, A., 1995. Factors affecting the reliability of hydrogen permeation measurement. *Materials Science Forum* 192-194, 63–78.
- Turnbull, A., Saenz de Santa Maria, M., Thomas, N.D., 1989. The effect of H<sub>2</sub>S concentration and pH on hydrogen permeation in AISI 410 stainless steel in 5% NaCl. *Corrosion Science* 29, 89–104.
- Van den Eeckhout, E., Laureys, A., Van Ingelgem, Y., Verbeken, K., 2017. Hydrogen permeation through deformed and heat-treated Armco pure iron. *Materials Science and Technology* 33, 1515–1523.
- Verbeken, K., 2012. Analysing hydrogen in metals: bulk thermal desorption spectroscopy (TDS) methods, in: Gangloff, R.P., Somerday, B.P. (Eds.), *Gaseous Hydrogen Embrittlement of Materials in Energy Technologies Vol. II*. Woodhead Publishing, pp. 27–55.
- Wang, S., Martin, M.L., Sofronis, P., Ohnuki, S., Hashimoto, N., Robertson, I.M., 2014. Hydrogen-induced intergranular failure of iron. *Acta Materialia* 69, 275–282.

- Yamabe, J., Awane, T., Matsuoka, S., 2015. Investigation of hydrogen transport behavior of various low-alloy steels with high-pressure hydrogen gas. *International Journal of Hydrogen Energy* 40, 11075–11086.
- Yamabe, J., Sezgin, J.G., Wada, K., 2021. Interpretation of complex, tensile-fracture phenomena in precipitation-hardened, martensitic stainless steels, 17-4PH, in presence of hydrogen. *Materials Science and Engineering: A* 823, 141717.
- Zafra, A., Belzunce, J., Rodríguez, C., 2020. Hydrogen diffusion and trapping in 42CrMo4 quenched and tempered steel: Influence of quenching temperature and plastic deformation. *Materials Chemistry and Physics* 255, 123599.